Rationally Designed Sodium Chromium Vanadium Phosphate Cathodes with Multi-Electron Reaction for Fast-Charging Sodium-Ion Batteries

Wei Zhang, Yulun Wu, Zhenming Xu,* Huangxu Li, Ming Xu, Jianwei Li, Yuhang Dai, Wei Zong, Ruwei Chen, Liang He, Zhian Zhang,* Dan J. L. Brett, Guanjie He,* Yanqing Lai,* and Ivan P. Parkin

Sodium super-ionic conductor (NASICON)-structured phosphates are emerging as rising stars as cathodes for sodium-ion batteries. However, they usually suffer from a relatively low capacity due to the limited activated redox couples and low intrinsic electronic conductivity. Herein, a reduced graphene oxide supported NASICON $Na_3Cr_{0.5}V_{1.5}(PO_4)_3$ cathode (VC/C-G) is designed, which displays ultrafast (up to 50 C) and ultrastable (1 000 cycles at 20 C) Na^+ storage properties. The VC/C-G can reach a high energy density of ≈470 W h kg^{-1} at 0.2 C with a specific capacity of 176 mAh g^{-1} (equivalent to the theoretical value); this corresponds to a three-electron transfer reaction based on fully activated V^{5+}/V^{4+}, V^{4+}/V^{3+}, V^{3+}/V^{2+} couples. In situ X-ray diffraction (XRD) results disclose a combination of solid-solution reaction and biphasic reaction mechanisms upon cycling. Density functional theory calculations reveal a narrow forbidden-band gap of 1.41 eV and a low Na^+ diffusion energy barrier of 0.194 eV. Furthermore, VC/C-G shows excellent fast-charging performance by only taking ≈11 min to reach 80% state of charge. The work provides a widely applicable strategy for realizing multi-electron cathode design for high-performance SIBs.

1. Introduction

Reducing carbon emissions is a world-wide and compulsory task for building a greener future. One approach using intermittent energy generation (solar/wind) urgently requires a reliable and cost-effective electrochemical energy storage technology.[1,2]

Lithium-ion batteries (LIBs) have changed modern life—enabling mobile communication and electric vehicles. They are the most widespread energy storage devices but they are not totally suitable for sustainable development due to the limited lithium resources in countries often with underlying political disputes.[3–5] As alternative candidates, sodium-ion batteries (SIBs) have drawn increasing attention by both academic and industrial communities on account of the high abundance of sodium resources.[6,7] Of great promise are inexpensive, high-energy, long-lifespan, and fast-charging SIBs in order to improve on LIBs.[8] However, a key bottleneck in commercializing SIBs is to identify competitive cathodes with long lifespan, negligible volume change, cost-effectiveness, as well as high capacity.[9–11]

Until now, several families of cathode materials have been developed for use such as layered oxides,[12,13] Prussian blues analogs,[14] and polyanion oxides.[15–17] Among these, sodium super-ionic conductor (NASICON)-structured $Na_xMeMe'(PO_4)_3$ (Me/Me' refers to transition metals) are capable of satisfying the above requirements in terms of high ionic conductivity (3D open frameworks), limited volume change (strong

W. Zhang, J. Li, Y. Dai, W. Zong, R. Chen, G. He, I. P. Parkin
Christopher Ingold Laboratory
Department of Chemistry
University College London
London WC1H 0AJ, UK
E-mail: g.he@ucl.ac.uk

W. Zhang, Y. Wu, L. He, Z. Zhang, Y. Lai
School of Metallurgy and Environment
Central South University
Changsha 410083, P. R. China
E-mail: zhangzhian@csu.edu.cn; laiyanqing@csu.edu.cn

The ORCID identification number(s) for the author(s) of this article can be found under https://doi.org/10.1002/aenm.202201065.

Z. Xu
Jiangsu Key Laboratory of Electrochemical Energy Storage Technologies
College of Materials Science and Technology
Nanjing University of Aeronautics and Astronautics
Nanjing 210016, P. R. China
E-mail: xuzhenming@nuaa.edu.cn

H. Li
Department of Chemistry
City University of Hong Kong, Kowloon
Hong Kong 999077, P. R. China

M. Xu
School of Chemistry
Xi'an Jiaotong University
Xi'an 710049, P. R. China

D. J. L. Brett, G. He
Department of Chemical Engineering
University College London
London WC1E 7JE, UK

P—O bonds), excellent air tolerance and higher redox potential (inductive effect between transition metal and phosphates).[18] Due to the ease of redox tunability, diverse NASI-CONs have been identified, including $Na_3V_2(PO_4)_3$,[19] $Na_2CrTi(PO_4)_3$,[20] $Na_2TiV(PO_4)_3$,[21,22] $Na_4NiV(PO_4)_3$,[23] $Na_3MnTi(PO_4)_3$,[24,25] $Na_3FeV(PO_4)_3$,[23] $Na_3MnZr(PO_4)_3$,[26] $Na_4MnV(PO_4)_3$,[23,27,28] $Na_4MnAl(PO_4)_3$,[29] $Na_4MnCr(PO_4)_3$,[30–32] and $Na_4VMn_{0.5}Fe_{0.5}(PO_4)_3$,[33] etc. Nevertheless, most NASICONs suffer from low capacity (<120 mAh g^{-1}) as a result of limited (i.e., one to two) electron transfer per chemical formula unit, which reduces the overall energy density and impedes further practical application. In this regard, it is a must to involve more electrons in redox reactions during cycling and thereby achieving higher capacity. Particularly, coupling transition metal elements with more redox reactions from the Me/Me′ sites of the NASICON structure is an indispensable rule when designing multi-electron transfer cathodes.[34] Among the reported transition metals in NASICONs, vanadium stands out as the most promising candidate by virtue of three readily available redox couples; V^{5+}/V^{4+}, V^{4+}/V^{3+}, and V^{3+}/V^{2+} at suitable electrochemical potentials. It is thus of great promise to completely activate these three redox couples in vanadium-based NASICONs.[34–36]

In addition, fast charging is emerging as a critical technology for practical application.[37–38] However, achieving fast charging for high-capacity cathodes remains a big challenge. To illustrate, stable structure, high ionic, and electronic conductivity are decisive factors when operating SIBs under high current density conditions.[39–41] NASICONs are intrinsically endowed with 3D open framework structure to readily diffuse Na^+ ($\approx10^{-13}$ to 10^{-8} cm^2 s^{-1}) with minimal phase transformation and low volume change ($\approx7\%$), which outperform that of layered oxides and Prussian blue analogs.[42,43] Therefore, NASICONs with high energy density would be an ideal choice for fast charging scenarios if the low electronic conductivity issue could be addressed.

Herein, we designed a reduced graphene oxide supported NASICON-type $Na_3Cr_{0.5}V_{1.5}(PO_4)_3$ material (VC/C-G) based on a simple sol-gel approach, which showed high-energy-density Na^+ storage performances with fast-charging properties. To be specific, the designed VC/C-G can reach a high energy density of ≈470 W h kg^{-1} at 0.2 C with a specific capacity of 176 mAh g^{-1}, which confirmed a three-electron reaction based on fully activated V^{5+}/V^{4+}, V^{4+}/V^{3+}, V^{3+}/V^{2+} redox couples. Furthermore, only ≈11 min were needed to reach 80% SOC. The underlying mechanisms for outstanding electrochemical performances were elucidated by galvanostatic intermittent titration technique (GITT), cyclic voltammetry (CV), and pseudocapacitance calculations. Additionally, operando X-ray diffraction (XRD) and X-ray photoelectron spectroscopy (XPS) were carried out to clarify structural evolutions as well as charge compensation mechanisms. Density functional theory (DFT) calculations revealed a narrow energy gap of 1.41 eV as well as a low sodium ion diffusion energy barrier of 0.194 eV, which explained the activated multi-electron reaction via partial introduction of Cr. This work provides a general strategy for multi-electron transfer and fast-charging cathode design for high-performance SIBs.

2. Results and Discussion

2.1. Material Characterizations

VC/C and VC/C-G were prepared by a common sol-gel approach (synthesis details could be found in Supporting Information). In Figure S1, Supporting Information, powder X-ray diffraction (XRD) was employed to determine their actual phases, in which the two samples belonged to R-3c space group with pure $Na_3Cr_{0.5}V_{1.5}(PO_4)_3$. The XRD Rietveld refinement provided detailed atomic occupation and structural information. As illustrated in **Figure 1**a, VC/C-G was endowed with a typical rhombohedral NASICON structure as confirmed by a low R_{wp} value of 3.86% (specific atom occupation and lattice parameters are listed in Table S1, Supporting Information). Particularly, as depicted in Figure 1b, V/Cr atoms occupy the same octahedral sites in a casual manner, while $[PO_4]$ tetrahedra are corner-shared with $[VO_6]/[CrO_6]$ octahedra to construct the basic "lantern" units $[Cr_{0.5}V_{1.5}(PO_4)_3]$. In this way, a 3D robust open-framework structure is built to readily diffuse Na^+ and is favorable for high rate capability.[34] The eight-coordinated Na(2) is favorable for uptake/insertion of Na^+. Likewise, the VC/C material possesses acceptable R_{wp} value of 3.99% (Figure S2 and Table S2, Supporting Information). Three Na^+ could be anticipated to insert/uptake to/from $Na_3Cr_{0.5}V_{1.5}(PO_4)_3$ based on the redox couples of V^{5+}/V^{4+}, V^{4+}/V^{3+}, and V^{3+}/V^{2+}, giving rise to a high theoretical capacity of 176 mAh g^{-1}, which surpasses that of most NASICON cathodes.[43]

Carbon coating is an efficient method to boost single particle electronic conductivity via organics pyrolysis. Reduced graphene oxide was adopted to construct a 3D interconnected conductive network as well so as to further enhance its electrochemical properties with a combination of intrinsic facile ion diffusion. From thermogravimetric analysis (TGA) in Figure S3, Supporting Information, the carbon contents were measured to be 10.3% (VC/C-G) and 9.5% (VC/C), respectively. We also used Raman spectroscopy to investigate the nature of carbon for both samples. In Figure S4, Supporting Information, two recognizable peaks at 1355 cm^{-1} (D-band) and 1580 cm^{-1} (G-band) were easily observed and their intensity ratios were 0.93 (VC/C-G) and 0.89 (VC/C), indicative of higher electronic conductivity of VC/C—G.[44] Fourier transform infrared spectra (FT-IR; Figure S5, Supporting Information) of these two samples are almost identical. The asymmetric and symmetric bending/stretching vibration signals of $[PO_4]$ tetrahedra and $[TiO_6]/[VO_6]$ octahedra could be found at ≈1000 cm^{-1}.[24,45] From X-ray photoelectron spectroscopy (XPS) results in Figure S6, Supporting Information, the existence of Cr, V, Na, P, O, C for both samples identified the elements on the surface. C 1s spectra (Figure S6b, Supporting Information) detected 3 bonding configurations such as O—C=O (289.1 eV), C—O (285.8 eV), and C—C (284.8 eV). Figure S6c,d, Supporting Information, show no apparent differences in V 2p and Cr 2p for both samples. Furthermore, Cr 2p and V 2p spectra determined the valences state of Cr^{3+} and V^{3+}.[32,42]

Moreover, transmission electron microscopy (TEM) was taken to investigate the morphology and microstructure of VC/C-G and VC/C. In Figure 1c–e, VC/C-G particles are uniformly coated by rGO layers with a reduced mean size of 0.1–1 µm compared with that of VC/C (4 µm; Figure S7,
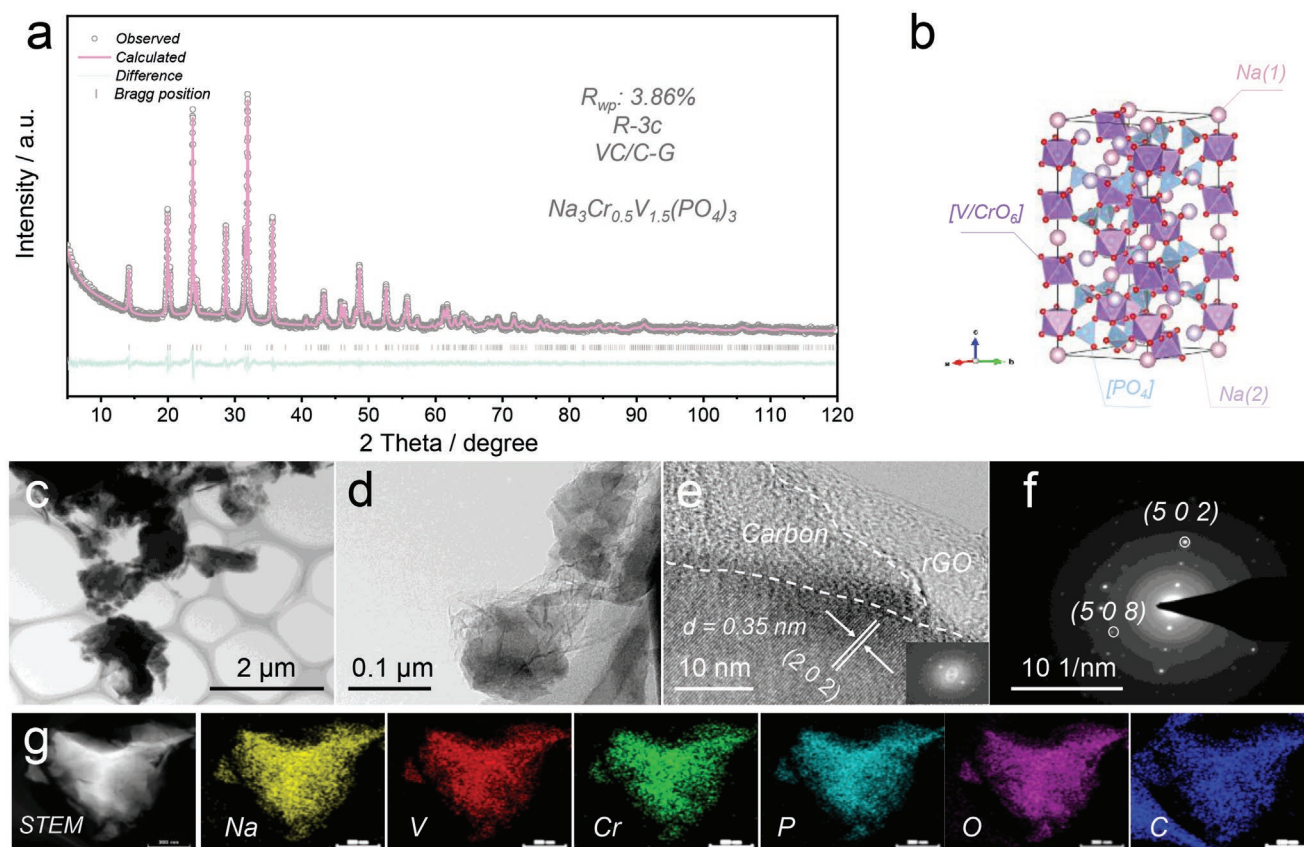
Figure 1. Characterizations of VC/C-G sample. a) XRD Rietveld refinement results and b) crystalline structure illustration. c,d) TEM and e) HRTEM images (inset: FFT image). f) SAED pattern. g) EDS mapping images.

Supporting Information), demonstrating that the rGO layer has a positive impact on decreasing the particle growth and hence shorter migration length for Na^+ (better kinetics) during sodiation/desodiation could be obtained. High-resolution TEM (HRTEM) image (Figure 1e) demonstrates that besides the rGO layer, a thin amorphous carbon layer was tightly coated on VC/C-G stemming from the pyrolysis of organic compounds upon sintering. Combined with rGO layer, they can provide 3D pathways for facile electron diffusion. Also, a lattice fringe of 0.35 nm can be observed, corresponding to the (2 0 2) lattice plane of $Na_3Cr_{0.5}V_{1.5}(PO_4)_3$. Selected area electron diffraction (SAED) in Figure 1f and Figure S7d, Supporting Information, further verified the well-crystallized VC/C-G and VC/C. Energy dispersive spectrometry (EDS; Figure 1g and Figure S7e, Supporting Information) mapping images demonstrate uniformly distributed Na, V, Cr, P, O, and C within VC/C-G and VC/C particles, in good accordance with the XRD and XPS results (Figure 1a; Figures S2 and S6, Supporting Information). Therefore, it can be concluded that VC/C and VC/C-G were successfully synthesized.

2.2. Electrochemical Performances

To evaluate the effectiveness of the designed structures, VC/C-G and VC/C cathode materials were fabricated in CR2032

coin cells with the Na metal as anodes. In **Figure 2**a, three evident voltage platforms of 4.02 V (V^{5+}/V^{4+}), 3.43 V (V^{4+}/V^{3+}), 1.65 V (V^{3+}/V^{2+}) could be easily observed for VC/C-G. Accordingly, it delivered 176 mAh g^{-1} (corresponding to the theoretical value) at 0.2 C (1 C = 100 mAh g^{-1}), which surpasses that of most NASICONs and confirms the full activation of three-electron redox reactions in $Na_3Cr_{0.5}V_{1.5}(PO_4)_3$. CV curves (Figure 2b) of VC/C-G identify three obvious reduction/oxidation couples, indicating outstanding kinetics of VC/C-G and serial evolutions of $NaCr_{0.5}V_{1.5}(PO_4)_3 \leftrightarrow Na_2Cr_{0.5}V_{1.5}(PO_4)_3 \leftrightarrow Na_3Cr_{0.5}V_{1.5}(PO_4)_3 \leftrightarrow Na_4Cr_{0.5}V_{1.5}(PO_4)_3$, which will be analyzed in detail in the following part. The negligible peak differences between the first and succeeding cycles of CV curves were due to the construction of solid electrolyte interphase (SEI) layer.[44] Moreover, the CV curves of VC/C-G were more keen-edged and more symmetric than that of VC/C (Figure S8, Supporting Information), demonstrating the enhanced redox kinetics due to the reduced Na^+ diffusion length and better electronic conductivity.

Rate performances are also significant for practical applications. In Figure 2c, VC/C showed 168 mAh g^{-1} at 0.2 C and 76 mAh g^{-1} at 50 C, still much higher than that of most NASICONs, which demonstrates the rationality of the as-designed VC/C as reference group. In comparison, VC/C-G displayed an outstanding rate capability: ultrahigh specific capacities of 176, 160.4, 152.8, 144.9, 141.2, 130.5, 113.4, 101.9, and 94.8 mAh g^{-1}
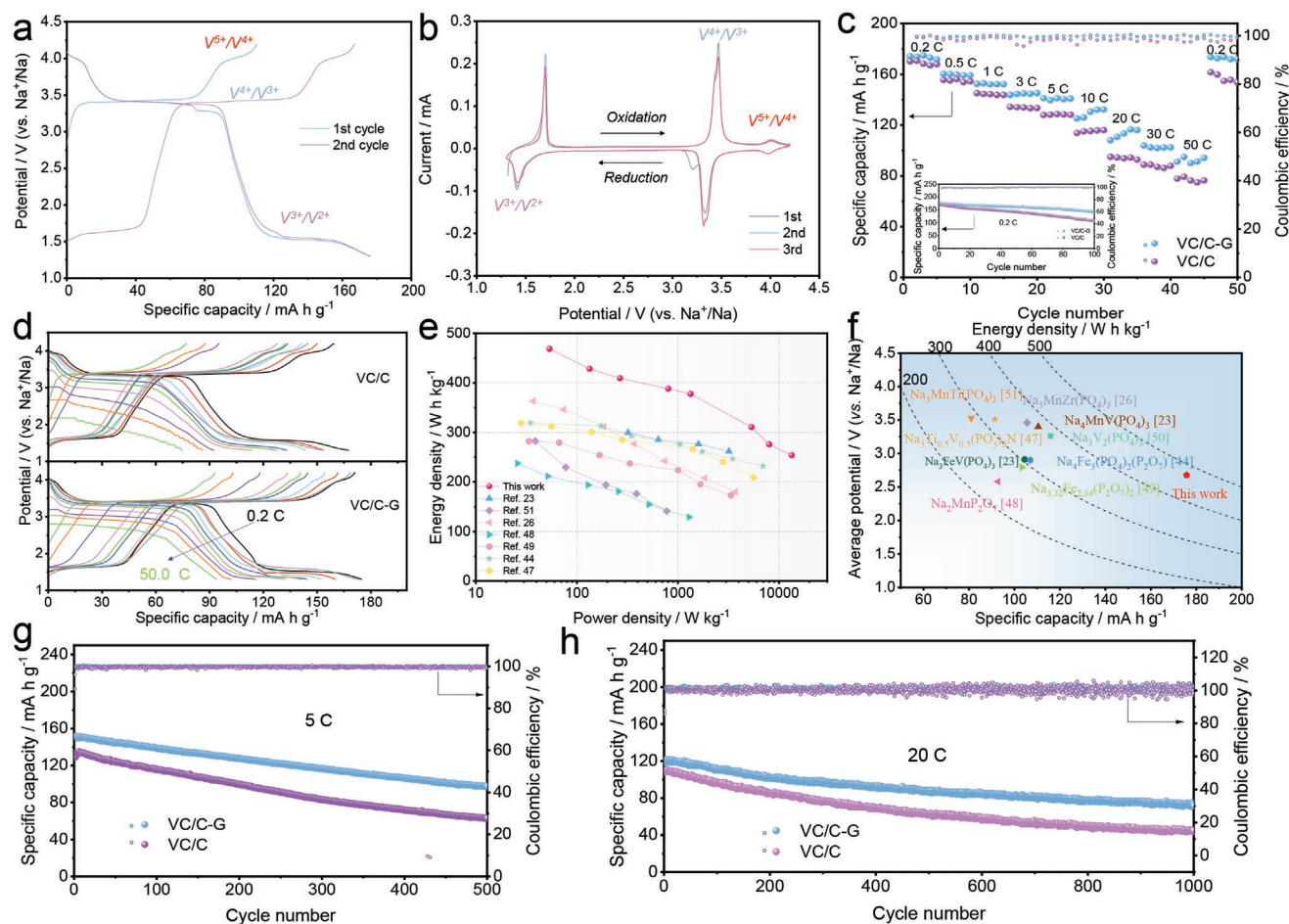
Figure 2. Electrochemical capabilities. a) Charge/discharge curves at 0.2 C. b) CV results of VC/C-G. c) Rate properties (inset: 0.2 C cycling ability) and d) corresponding charge/discharge profiles. e) Ragone plots. f) Comparison among VC/C-G and various materials with regard to specific capacity, average potential, and energy density. Cycling performances at g) 5 C and h) 20 C, respectively.

is achieved at various current densities of 0.2, 0.5, 1.0, 3.0, 5.0, 10.0, 20.0, 30.0, and 50.0 C, respectively. When the rate returned to 0.2 C, the high capacity of 173.6 mAh g^{-1} can still be recovered, indicating an excellent reversibility. In comparison with VC/C, the modified VC/C-G electrode exhibits much improved rate performances under various C-rates (particularly high rates). Furthermore, Figure 2d shows a suppressed electrochemical polarization of VC/C-G.[44,46] We also make a comparison with other cathode materials in terms of energy density and power density based on half cells.[23,26,44,47–51] The Ragone plots (Figure 2e) of VC/C-G demonstrates a remarkable power capability. As for Figure 2f, VC/C-G shows a higher energy density of ≈470 W h kg^{-1}, outweighing that of most other polyanion oxides.

The cycling stabilities at different current densities of 0.2, 5, and 20 C, respectively were explored. Overall, VC/C-G exhibited steady and boosted cyclabilities. As shown in the inset of Figure 2c, VC/C-G displayed an initial capacity of 175.8 mAh g^{-1} and still maintained 141.5 mAh g^{-1} after 100 cycles under 0.2 C. However, VC/C could only deliver 107.3 mAh g^{-1} under identical conditions. Also, the batteries were subjected to 5 C (Figure 2g) so as to study the long-term cycling capabilities. Markedly, VC/C-G possessed an acceptable capacity of 97.7 mAh g^{-1}

after 500 cycles while VC/C only showed 63.1 mAh g^{-1} at this rate. As illustrated in Figure 2h, VC/C-G could steadily cycle 1000 times at a high rate of 20 C with a higher capacity retention. On the other hand, VC/C merely possessed 41% capacity retention. The long lifespan demonstrated the potential of the as-synthesized cathodes for practical application.

2.3. Kinetics Properties

For the purpose of clarifying the origin of enhanced rate performances and excellent cycling stability, we further studied the kinetics properties. First, galvanostatic intermittent titration technique (denoted as GITT) was carried out to determine the sodium ion diffusion coefficient (D_{Na+}) after initial activation cycles. As shown in **Figure 3**a, D_{Na+} of VC/C-G turned out to be 10^{-11} to 10^{-8} cm^2 s^{-1}, which outweighs those of most reported materials and is conducive to good rate properties.[34] Moreover, the overpotential was investigated, which refers to the voltage difference between relaxed potential and titrated cut-off potential. The small overpotential of 10^{-9} to 10^{-11} V in the whole range further supported the ion diffusion coefficient results.
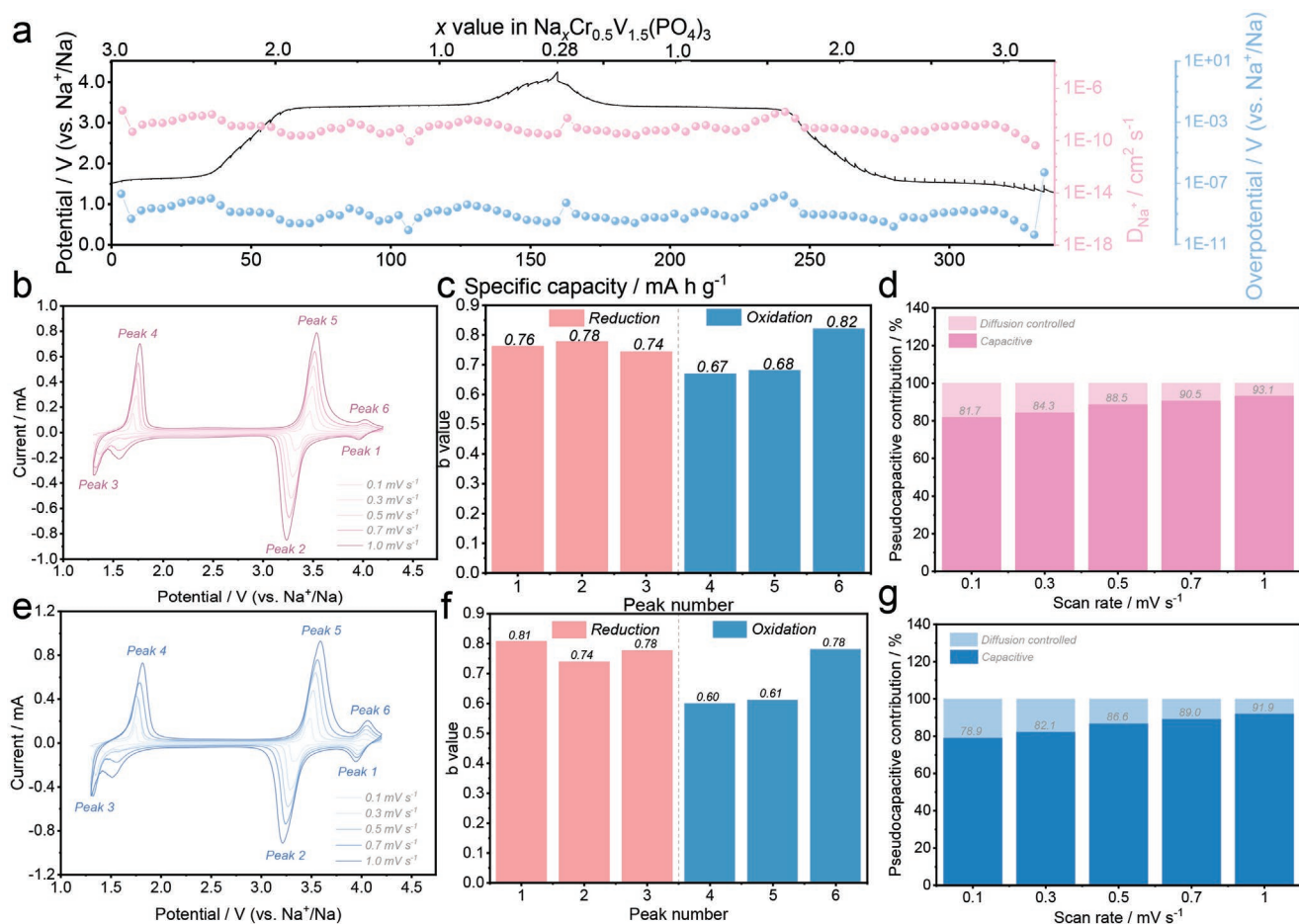
Figure 3. Kinetics performances. a) GITT profiles, D_{Na+}, and overpotentials of VC/C-G. b) CV curves from 0.1 to 1.0 mV s^{-1}, c) corresponding b values, and d) capacitance contributions of VC/C-G. e) CV curves at 0.1–1.0 mV s^{-1}, f) corresponding b values, and g) capacitance contributions of VC/C.

In addition, the pseudocapacitive contribution cannot be neglected when small particle size and Cr dopant are taken into consideration, which has a big impact on rate capabilities and prolonged lifespan. In general, two processes are involved in sodiation/desodiation: i) common Faradic processes (diffusion-controlled redox reactions), which confirm a fixed potential; ii) non-Faradic processes (surface-controlled redox reactions), which have a positive impact on rate performance and extended life expectancy. We subjected the two electrodes to various rates via CV approaches (Figure 3b,e). It has been widely accepted that b value ranging from 0.5 to 1 indicates fast kinetics of battery materials and means that the Na$^+$ storage is dominated by both the diffusion-controlled and surface-controlled behaviors.[52] From Figure 3c,f, the measured b values were approximately 0.6–0.8 for all peaks, signals of partial pseudocapacitance effect.[52] The pseudocapacitive contribution of VC/C-G at 0.1 mV s^{-1} was 81.7%, larger than that of VC/C as indicated in Figures S9 and S10, Supporting Information. Obviously, an increasing trend of this contribution can be observed for VC/C-G and VC/C when scan rates are elevated (Figure 3d,g; the calculation details were specified in Supporting Information). As for the whole scan range, VC/C-G possessed higher pseudocapacitive contributions and eventually achieved 93.1% at 1.0 mV s^{-1}. Accordingly, non-Faradic process can play a pivotal role in the extended lifespan and improved rate properties.

2.4. Sodium-Ion Storage Mechanism

To further disclose the sodium-ion storage mechanism and structural evolutions, operando XRD was carried out based on a well-designed cell which was subjected to different potential at a fixed current density (as seen in the left side of **Figure 4**a,b). The full-scope patterns are depicted in Figure S12, Supporting Information. As shown in Figure 4a,b, the major reflections corresponding to (10$\bar{2}$), (104), (2$\bar{1}$0), (2$\bar{1}$3), (20$\bar{4}$), (2$\bar{1}$6), (3$\bar{1}$2), and (300) could be obviously noted. Generally speaking, all of them undergo highly reversible changes when cycling, which confirms the robust NASICON framework structure and the good reversible electrochemical performances as discussed above. During the initial stage, the peaks were all indexed to a rhombohedral phase with the R-3c space group. Upon first charging, all reflections gradually shifted to higher angles, indicating that a solid-solution reaction was involved and the structure underwent a shrinkage except that the signal of (2$\bar{1}$6) vanished briefly. According to previous reports, it proves a biphasic reaction.[22,30] The same is confirmed by the following symmetrical discharging area. As discharging proceeds to the low cut-off potential, the (2$\bar{1}$6) appeared again and all peaks moved to lower 2θ values, demonstrating a combination of biphasic and solid-solution mechanisms. Likewise, the peaks in
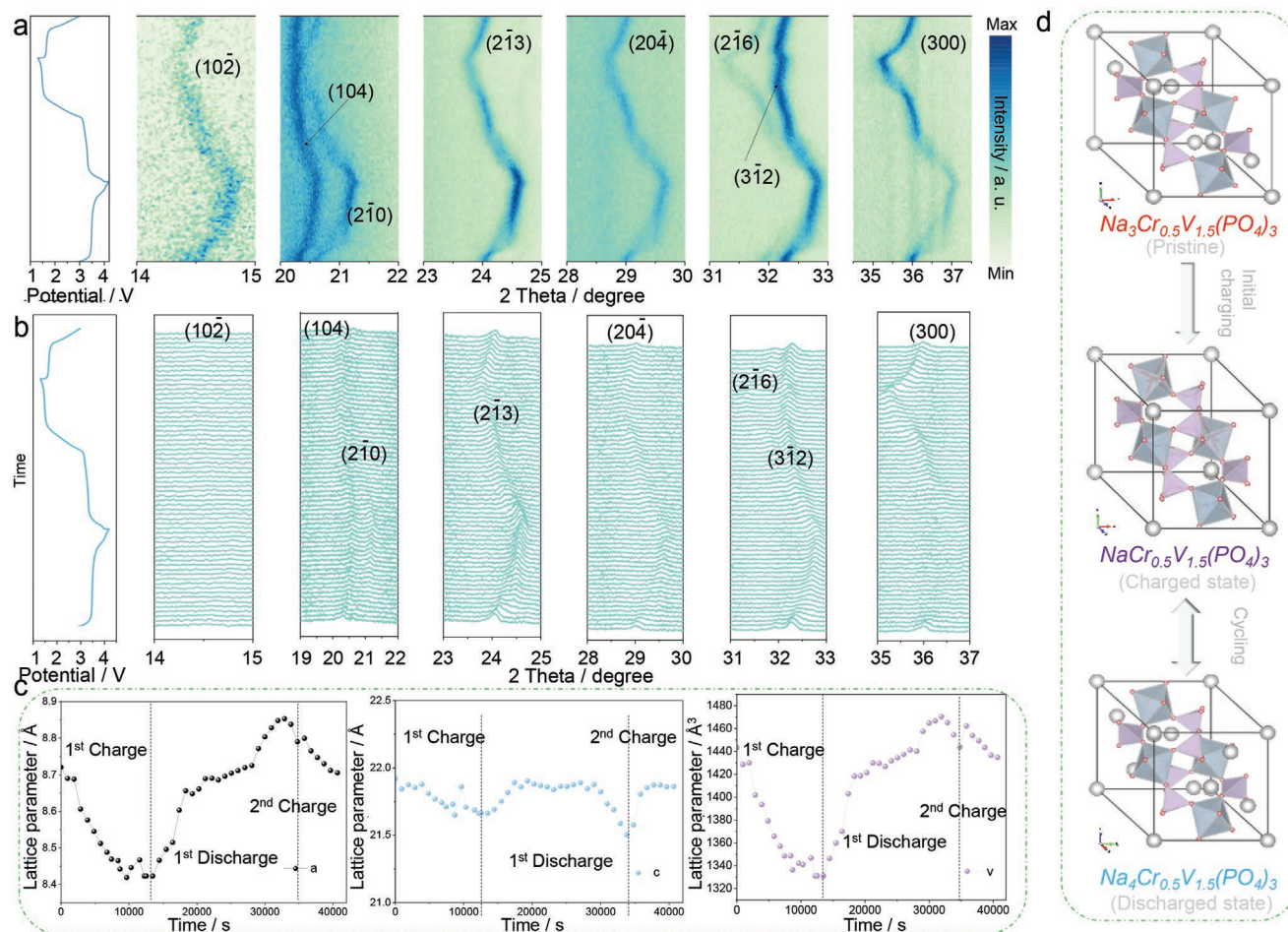
Figure 4. a) In situ XRD contour patterns and b) stacked line plots of $Na_3Cr_{0.5}V_{1.5}(PO_4)_3$ upon cycling. c) Corresponding changes of lattice parameters. d) Schematic illustration of the crystal structure of $Na_3Cr_{0.5}V_{1.5}(PO_4)_3$ at different charging states.

succeeding charging processes displayed a right shift to the initial peak positions, which can be ascribed to the solid-solution mechanism and show a highly reversible structural flexibility. Hence, in situ XRD results further verified that through Na^+ storage process the cathode experiences combined biphasic and solid-solution mechanisms for $Na_3Cr_{0.5}V_{1.5}(PO_4)_3$; the solid-solution reactions stand out as the main reaction mechanisms, which are inducive to the good electrochemical reversibility and fast Na^+ diffusion. The remained Na^+ in the unit cell (at the deep charged state) serves as the binding pillars to stabilize the crystal structure.

Furthermore, as illustrated in Figure 4c, we collected the lattice parameters at various charge states so as to obtain a clearer picture about the structure evolution. Evidently, a (=b)-axis, c-axis decreased and therefore v (volume) experienced a declining trend in the first charging process. Upon discharging, the a-axis tended to increase while c-axis underwent a negligible change. Thus, c-axis showed a similar trend with a-axis. As the second charging proceeds, a-axis and c-axis displayed an opposite evolution. Consequently, the volume change of $Na_3Cr_{0.5}V_{1.5}(PO_4)_3$ was measured to be 7.79%, which is comparable to that of typical NASICONs.[28,32] Such a sturdy NASICON structure is beneficial to its outstanding

electrochemical stability. Combined with the above discussions, the structural transformations of $Na_3Cr_{0.5}V_{1.5}(PO_4)_3$ are illustrated in Figure 4d. During the extraction of the first two Na^+ ions from $Na_3Cr_{0.5}V_{1.5}(PO_4)_3$, the pristine state was transformed to $Na_1Cr_{0.5}V_{1.5}(PO_4)_3$. Upon the subsequent cycling, three Na^+ ions in total were inserted to form $Na_4Cr_{0.5}V_{1.5}(PO_4)_3$, which is consistent with the multielectron electrochemical properties (Figure 2 and Figure 3a).

Additionally, XPS was adopted to further confirm charge compensation mechanism of $Na_3Cr_{0.5}V_{1.5}(PO_4)_3$ at different voltage (Figure S13, Supporting Information). The changes of $Na_3Cr_{0.5}V_{1.5}(PO_4)_3$ → $Na_1Cr_{0.5}V_{1.5}(PO_4)_3$, and $Na_1Cr_{0.5}V_{1.5}(PO_4)_3$ ↔ $Na_2Cr_{0.5}V_{1.5}(PO_4)_3$ ↔ $Na_3Cr_{0.5}V_{1.5}(PO_4)_3$ ↔ $Na_4Cr_{0.5}V_{1.5}(PO_4)_3$ are presumed to accompany with the transformations of transition metal's valence states. As displayed in Figure S13, Supporting Information, the first binding energy of V $2p_{3/2}$ was 516.82 eV (V^{3+}).[53] When charged to 3.72 V, it shifted to 517.00 eV (V^{4+}).[21,54] Subsequently, when it was subjected to 4.2 V, the peak of V $2p_{3/2}$ further experienced a right shift to 517.40 eV (V^{5+}).[55] As discharging proceeds to 3.60 and 2.30 V, valence states of V returned to V^{4+} and V^{3+}, respectively.[21,53–54] After that, the peak of V $2p_{3/2}$ further shifted to 516.50 eV (V^{2+}).[56] On the other hand, the peaks of Cr $2p_{3/2}$

ADVANCED
SCIENCE NEWS

www.advancedsciencenews.com

ADVANCED
ENERGY
MATERIALS

www.advenergymat.de

were kept invariant (577.71 eV, signal of Cr^{3+}) throughout the whole process.[57] The above analysis further verified the illustration in Figure 4d.

2.5. DFT Calculations

To further understand its intrinsic physicochemical capabilities as well as superior dynamics and kinetics from a theoretical perspective, density functional theory (DFT) calculations were conducted. As shown in **Figure 5**a, a convex-hull phase diagram was created, which is based on the formation energy under different concentrations of Na^+ in $Na_xCr_{0.5}V_{1.5}(PO_4)_3$ and depicts the structural changes upon cycling.[46] It could be deduced that $Na_3Cr_{0.5}V_{1.5}(PO_4)_3$ stands out as the most stable phase thermodynamically, and all the metastable phases ranging from $Na_0Cr_{0.5}V_{1.5}(PO_4)_3$ to $Na_4Cr_{0.5}V_{1.5}(PO_4)_3$ could be electrochemically obtained due to the negative formation energies, supporting the multielectron redox behaviors as discussed above. We also calculated the voltage profiles (Figure 5b) in terms of V^{5+}/V^{4+}, V^{4+}/V^{3+}, and V^{3+}/V^{2+}, which agreed well with the experimental results except for some negligible deviation. Additionally, the total and partial density of states (DOS) diagram are shown in Figure 5c.

Apparently, the valence bands were made of the hybridized Na 3s, V 3d, Cr 3d, P 2p, and O 2p orbitals. The forbidden band gap was calculated to be 1.41 eV, which is even lower than that of the typical NASICON-$Na_3V_2(PO_4)_3$ ($\approx$2.3 eV) and hence contributes to the boosted electronic conductivity for $Na_3Cr_{0.5}V_{1.5}(PO_4)_3$.[36] The lowered band gap could be regarded as a consequence of one more valence electron of Cr ($[Ar]3d^54s^1$) as compared to that of V ($[Ar]3d^34s^2$). Also, it may be an intrinsic reason for the activated high-potential V^{5+}/V^{4+} in $Na_3Cr_{0.5}V_{1.5}(PO_4)_3$.

To further decipher the inherent features that could account for the superior rate performances, we carried out both bond valence (BV) and nudged elastic band (NEB) calculations to probe its ion migration behaviors. The BV approach is a widely-used empirical method for the initial identification of ionic diffusion pathways (Figure 5d).[46] It is clear that $Na_3Cr_{0.5}V_{1.5}(PO_4)_3$ possesses 3D diffusion pathways for sodium ions on account of the well-interconnected lowest energy regions. As such, an NEB study was further conducted to investigate the barrier energy. As illustrated in Figure 5e, all Na^+ diffusion pathways were classified as four different types in total hinged on various Na^+ local environments. From Figure 5f, the well-interconnected 3D pathways contribute to relatively low energy barriers no more than 0.396 eV, which are lower than those of the well-studied
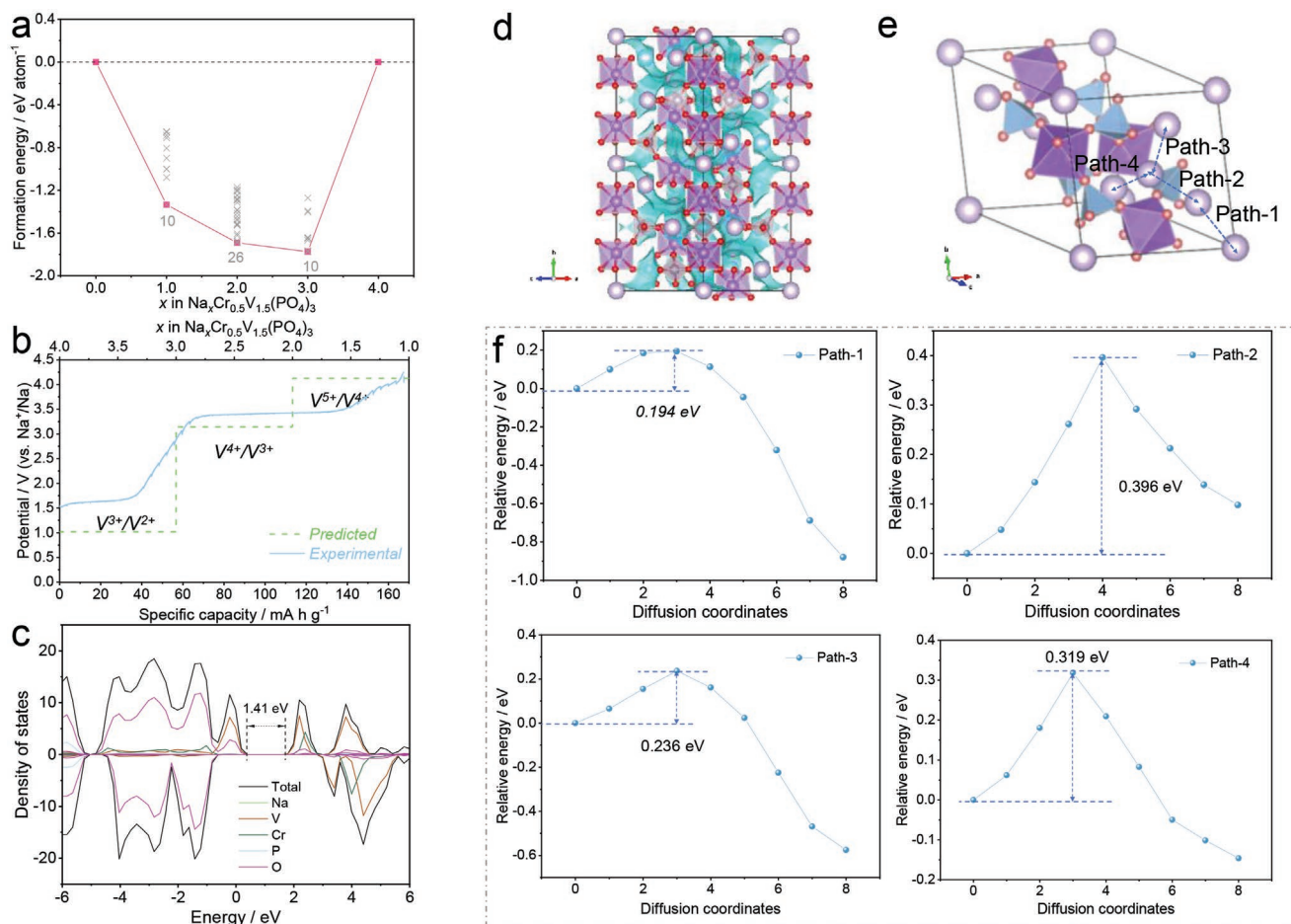

Figure 5. DFT calculations of $Na_3Cr_{0.5}V_{1.5}(PO_4)_3$. a) Convex-hull phase diagram and b) the calculated voltage profiles. c) Total and partial DOS. d) BV map of Na ions. e) Sodium-ion diffusion pathways and f) the corresponding migration energy barriers.

$Na_3V_2(PO_4)_3$ and other NASICONs.[21,31,35,36] It offers valid evidence for the high Na^+ diffusion coefficient as discussed in Figure 3a and therefore accounts for the activated V^{5+}/V^{4+} from a kinetics perspective.

Hence, through partial introduction of Cr, the forbidden band gap and the Na^+ migration energy barrier could be decreased, which may be the intrinsic reason for the activated high-potential V^{5+}/V^{4+} in $Na_3Cr_{0.5}V_{1.5}(PO_4)_3$. Compared with Cr-free $Na_3V_2(PO_4)_3$ (Figures S20–S24, Supporting Information), the activated V^{5+}/V^{4+} redox couple in $Na_3Cr_{0.5}V_{1.5}(PO_4)_3$ is thereby beneficial for the improved energy density, better rate performances, and boosted cycling stability (Figure 2).

2.6. Fast-Charging Performances

Fast-charging properties were investigated using a high constant-current (CC) charging protocol (1, 3, and 5 C) with a fixed normal CC discharging rate (1 C). From **Figure 6**a and Figure S14, Supporting Information, there is an increasing trend for the voltage platforms with an increasing charging rate, which can be ascribed to the electrochemical polarization. Also,

VC/C-G showed much more overlapped profiles than VC/C, which indicates a better kinetics of VC/C-G and is in agreement with the results in Figures 2 and 3. The dQ/dV plots of VC/C-G (Figure 6d) displayed more symmetrical curves than that of VC/C (Figure S15, Supporting Information). We further made a comparison for these two samples in terms of the charging time to reach the same state of charge (SOC) under different charging rate. As displayed in Figure 6b,c, it took a shorter period to get to the anticipated SOC for VC/C-G at all current rates. To be specific, it needed 87 min for VC/C to reach 100% SOC at 1 C (25 min at 3 C) while it only took 73.3 min (22.7 min at 3 C) for VC/C-G under the same condition. Even under a higher charging rate of 5 C, it only took 2.6 min for VC/C-G to reach 20% SOC and 10.7 min to get to 80% SOC but VC/C spent 3 min (20% SOC) and 11.8 min (80% SOC), respectively. The above results demonstrate that our well-designed cathode materials for SIBs are of paramount potential to meet practical requirements for fast-charging scenarios. On the other hand, fast-charging cycling ability plays a crucial role in battery operation. As shown in Figure 6e-f and Figure S16, Supporting Information, VC/C-G displayed much more stable cycling performances, when subjected to different charging rates (1, 3, and
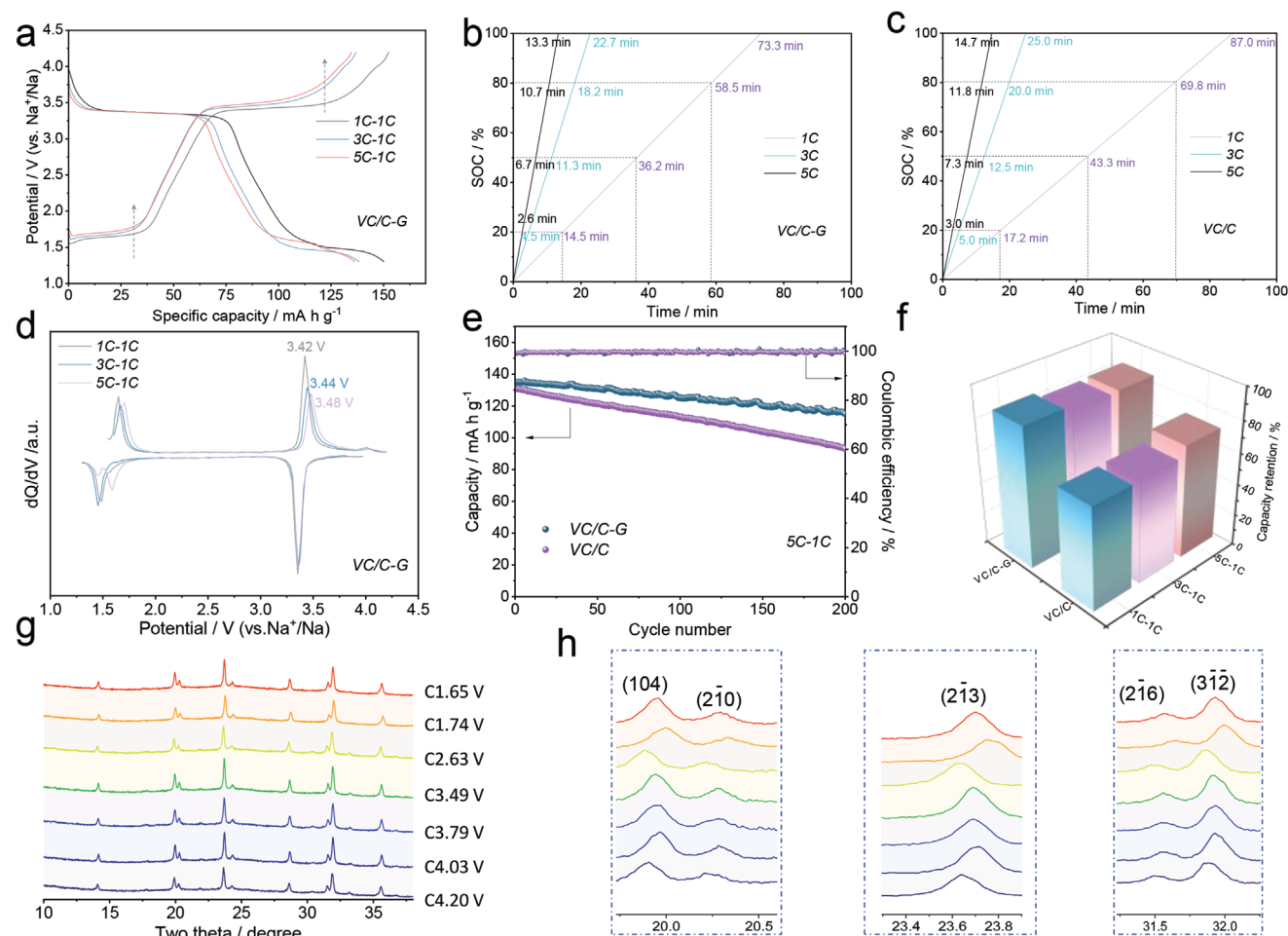

Figure 6. Fast-charging performances. a) Charge-discharge curves of VC/C-G at different charging rates with a fixed discharging rate of 1 C. SOC-time plots of b) VC/C-G and c) VC/C. dQ/dV plots of d) VC/C-G. e) Fast-charging cycling performances at 5 C- 1 C. f) Summary of capacity retentions at different charging rates. g) Ex situ XRD results of VC/C-G at the charging rate of 5 C and h) corresponding enlarged patterns.

5 C) with a fixed discharging rate of 1 C though they delivered similar initial capacities. From Figure 6f, the capacity retentions for VC/C-G are 88.79% (100 cycles), 85.24% (200 cycles), 86% (200 cycles) at 1 C- 1 C, 3 C- 1C, and 5 C-1 C, respectively. However, VC/C only retained 65.04%, 65.37%, 71.66% of initial capacities under the same conditions. Furthermore, we conducted ex situ XRD to study structural transformations with a fast-charging rate of 5 C. As displayed in Figure 6g,h and Figure S17, Supporting Information, they experienced highly reversible and negligible peak shifts with a near-zero volume change of 0.33% (Figure S18, Supporting Information). Such a value seems to be contradictory to that of the former low-current in situ XRD results in Figure 4. We think large capacitive contributions could account for this, especially, under such high charging rate. Hence, the combination of a robust 3D framework structure, facile ionic pathways, 3D conductive network, and large capacitive contributions can account for the excellent battery performances, which paves the way for its future application.

3. Conclusion

In summary, we have successfully designed a reduced graphene oxide supported NASICON-$Na_3Cr_{0.5}V_{1.5}(PO_4)_3$. When served as a cathode for SIBs, the material demonstrated ultrafast and ultrastable Na^+ storage performances based on fully activated V^{5+}/V^{4+}, V^{4+}/V^{3+}, V^{3+}/V^{2+} redox couples with good fast-charging properties. Specifically, the designed material can reach a high energy density of ≈470 W h kg^{-1} with a reversible capacity of 176 mAh g^{-1} (corresponding to theoretical value) at 0.2 C and an outstanding rate capability up to 50 C as well as superior good cyclability of 1000 cycles even at 20 C. And only a short time of ≈11 min was needed to get to 80% SOC. In addition, in situ XRD results showed that a combined solid-solution and biphasic reaction mechanism was involved in Na^+ storage process. DFT calculations revealed a narrow forbidden-band gap of 1.41 eV as well as a low Na^+ diffusion energy barrier of 0.194 eV, which accounted for the activated multi-electron reaction through partial introduction of Cr. Our work provides a general strategy for realizing multi-electron cathodes design for high-performance SIBs.

Supporting Information

Supporting Information is available from the Wiley Online Library or from the author.

Acknowledgements

Conflict of Interest

The authors declare no conflict of interest.

Data Availability Statement

The data that support the findings of this study are available from the corresponding author upon reasonable request.

[1] Y. Tian, G. Zeng, A. Rutt, T. Shi, H. Kim, J. Wang, J. Koettgen, Y. Sun, B. Ouyang, T. Chen, Z. Lun, Z. Rong, K. Persson, G. Ceder, *Chem. Rev.* **2021**, *121*, 1623.

[2] W. Zong, H. Guo, Y. Ouyang, L. Mo, C. Zhou, G. Chao, J. Hofkens, Y. Xu, W. Wang, Y. E. Miao, G. He, I. P. Parkin, F. Lai, T. Liu, *Adv. Funct. Mater.* **2021**, *32*, 2110016.

[3] F. Wu, J. Maier, Y. Yu, *Chem. Soc. Rev.* **2020**, *49*, 1569.

[4] J. Li, B. Zhu, S. Li, D. Wang, W. Zhang, Y. Xie, J. Fang, J. Hong, Y. Lai, Z. Zhang, *J. Electrochem. Soc.* **2021**, *168*, 080510.

[5] Y. Dai, Q. Li, S. Tan, Q. Wei, Y. Pan, X. Tian, K. Zhao, X. Xu, Q. An, L. Mai, Q. Zhang, *Nano Energy* **2017**, *40*, 73.

[6] R. Usiskin, Y. Lu, J. Popovic, M. Law, P. Balaya, Y.-S. Hu, J. Maier, *Nat. Rev. Mater.* **2021**, *6*, 1020.

[7] S. Tan, S. Jiang, Q. Wei, Q. Huang, Y. Dai, F. Xiong, Q. Li, Q. An, X. Xu, Z. Zhu, X. Bai, L. Mai, *Adv. Mater.* **2018**, *30*, 1707122.

[8] J.-M. Tarascon, *Joule* **2020**, *4*, 1616.

[9] F. Wu, C. Zhao, S. Chen, Y. Lu, Y. Hou, Y.-S. Hu, J. Maier, Y. Yu, *Mater. Today* **2018**, *21*, 960.

[10] S. Chu, S. Guo, H. Zhou, *Chem. Soc. Rev.* **2021**, *50*, 13189.

[11] H. Li, W. Zhang, K. Sun, J. Guo, K. Yuan, J. Fu, T. Zhang, X. Zhang, H. Long, Z. Zhang, Y. Lai, H. Sun, *Adv. Energy Mater.* **2021**, *11*, 2100867.

[12] Y. Huang, Y. Zhu, A. Nie, H. Fu, Z. Hu, X. Sun, S. C. Haw, J. M. Chen, T. S. Chan, S. Yu, G. Sun, G. Jiang, J. Han, W. Luo, Y. Huang, *Adv. Mater.* **2022**, *34*, 2105404.

[13] C. Zhao, Q. Wang, Z. Yao, J. Wang, B. Sánchez-Lengeling, F. Ding, X. Qi, Y. Lu, X. Bai, B. Li, H. Li, A. Aspuru-Guzik, X. Huang, C. Delmas, M. Wagemaker, L. Chen, Y.-S. Hu, *Science* **2020**, *370*, 708.

[14] J. Song, L. Wang, Y. Lu, J. Liu, B. Guo, P. Xiao, J.-J. Lee, X.-Q. Yang, G. Henkelman, J. B. Goodenough, *J. Am. Chem. Soc.* **2015**, *137*, 2658.

[15] Y. Cao, C. Yang, Y. Liu, X. Xia, D. Zhao, Y. Cao, H. Yang, J. Zhang, J. Lu, Y. Xia, *ACS Energy Lett.* **2020**, *5*, 3788.

[16] T. Wang, W. Zhang, H. Li, J. Hu, Y. Lai, Z. Zhang, *ACS Appl. Energy Mater.* **2020**, *3*, 3845.

[17] H. Li, C. Guan, M. Xu, J. Guo, K. Yuan, K. Cheng, Y. Xie, L. Zhang, J. Zheng, Y. Lai, Z. Zhang, *Energy Storage Mater.* **2022**, *47*, 526.

[18] Q. Zhou, L. Wang, W. Li, K. Zhao, M. Liu, Q. Wu, Y. Yang, G. He, I. P. Parkin, P. R. Shearing, D. J. L. Brett, J. Zhang, X. Sun, *Electrochem. Energy Rev.* **2021**, *4*, 793.

[19] H. Xiong, G. Sun, Z. Liu, L. Zhang, L. Li, W. Zhang, F. Du, Z. A. Qiao, *Angew. Chem., Int. Ed.* **2021**, *60*, 10334.

[20] K. Kawai, D. Asakura, S.-i. Nishimura, A. Yamada, *Chem. Commun.* **2019**, *55*, 13717.

[21] W. Zhang, Z. Xu, H. Li, M. Xu, S. Wang, Z. Li, A. Wang, L. Zhang, L. He, S. Li, B. Zhu, Z. Zhang, Y. Lai, *Chem. Eng. J.* **2022**, *433*, 133542.

[22] D. Wang, X. Bie, Q. Fu, D. Dixon, N. Bramnik, Y. S. Hu, F. Fauth, Y. Wei, H. Ehrenberg, G. Chen, F. Du, *Nat. Commun.* **2017**, *8*, 15888.

[23] W. Zhou, L. Xue, X. Lü, H. Gao, Y. Li, S. Xin, G. Fu, Z. Cui, Y. Zhu, J. B. Goodenough, *Nano Lett.* **2016**, *16*, 7836.

[24] H. Li, M. Xu, C. Gao, W. Zhang, Z. Zhang, Y. Lai, L. Jiao, *Energy Storage Mater.* **2020**, *26*, 325.

[25] H. Li, W. Zhang, Z. Han, K. Sun, C. Gao, K. Cheng, Z. Liu, Q. Chen, J. Zhang, Y. Lai, Z. Zhang, H. Sun, *Mater. Today Energy* **2021**, *21*, 100754.

[26] H. Gao, I. D. Seymour, S. Xin, L. Xue, G. Henkelman, J. B. Goodenough, *J. Am. Chem. Soc.* **2018**, *140*, 18192.

[27] W. Zhang, Z. Zhang, H. Li, D. Wang, T. Wang, X. Sun, J. Zheng, Y. Lai, *ACS Appl. Mater. Interfaces* **2019**, *11*, 35746.

[28] C. Xu, R. Xiao, J. Zhao, F. Ding, Y. Yang, X. Rong, X. Guo, C. Yang, H. Liu, B. Zhong, Y.-S. Hu, *ACS Energy Lett.* **2022**, *7*, 97.

[29] Q. Wang, C. Ling, J. Li, H. Gao, Z. Wang, H. Jin, *Chem. Eng. J.* **2021**, *425*, 130680.

[30] J. Wang, Y. Wang, D. H. Seo, T. Shi, S. Chen, Y. Tian, H. Kim, G. Ceder, *Adv. Energy Mater.* **2020**, *10*, 1903968.

[31] W. Zhang, H. Li, Z. Zhang, M. Xu, Y. Lai, S.-L. Chou, *Small* **2020**, *16*, 2001524.

[32] J. Zhang, Y. Liu, X. Zhao, L. He, H. Liu, Y. Song, S. Sun, Q. Li, X. Xing, J. Chen, *Adv. Mater.* **2020**, *32*, 1906348.

[33] C. Xu, J. Zhao, E. Wang, X. Liu, X. Shen, X. Rong, Q. Zheng, G. Ren, N. Zhang, X. Liu, X. Guo, C. Yang, H. Liu, B. Zhong, Y. S. Hu, *Adv. Energy Mater.* **2021**, *11*, 2100729.

[34] H. Li, M. Xu, Z. Zhang, Y. Lai, J. Ma, *Adv. Funct. Mater.* **2020**, *28*, 2000473.

[35] Y. Zhao, X. Gao, H. Gao, H. Jin, J. B. Goodenough, *Adv. Funct. Mater.* **2020**, *30*, 1908680.

[36] M. Chen, W. Hua, J. Xiao, J. Zhang, V. W. Lau, M. Park, G. H. Lee, S. Lee, W. Wang, J. Peng, L. Fang, L. Zhou, C. K. Chang, Y. Yamauchi, S. Chou, Y. M. Kang, *J. Am. Chem. Soc.* **2021**, *143*, 18091.

[37] W. Cai, Y.-X. Yao, G.-L. Zhu, C. Yan, L.-L. Jiang, C. He, J.-Q. Huang, Q. Zhang, *Chem. Soc. Rev.* **2020**, *49*, 3806.

[38] Y. Liu, Y. Zhu, Y. Cui, *Nat. Energy* **2019**, *4*, 540.

[39] D. Chao, R. DeBlock, C. H. Lai, Q. Wei, B. Dunn, H. J. Fan, *Adv. Mater.* **2021**, *33*, 2103736.

[40] Q. Ni, L. Zheng, Y. Bai, T. Liu, H. Ren, H. Xu, C. Wu, J. Lu, *ACS Energy Lett.* **2020**, *5*, 1763.

[41] S. Wang, H. Li, W. Zhang, J. Zheng, S. Li, J. Hu, Y. Lai, Z. Zhang, *ACS Appl. Energy Mater.* **2021**, *4*, 10136.

[42] H. Li, T. Jin, X. Chen, Y. Lai, Z. Zhang, W. Bao, L. Jiao, *Adv. Energy Mater.* **2018**, *8*, 1801418.

[43] R. Rajagopalan, Z. Zhang, Y. Tang, C. Jia, X. Ji, H. Wang, *Energy Storage Mater.* **2021**, *34*, 171.

[44] M. Chen, W. Hua, J. Xiao, D. Cortie, W. Chen, E. Wang, Z. Hu, Q. Gu, X. Wang, S. Indris, S. L. Chou, S. X. Dou, *Nat. Commun.* **2019**, *10*, 1480.

[45] D. Wang, Z. Wei, Y. Lin, N. Chen, Y. Gao, G. Chen, L. Song, F. Du, *J. Mater. Chem. A* **2019**, *7*, 20604.

[46] M. Chen, W. Hua, J. Xiao, D. Cortie, X. Guo, E. Wang, Q. Gu, Z. Hu, S. Indris, X. Wang, S. Chou, S. Dou, *Angew. Chem., Int. Ed.* **2020**, *132*, 2470.

[47] M. Chen, J. Xiao, W. Hua, Z. Hu, W. Wang, Q. Gu, Y. Tang, S. L. Chou, H. K. Liu, S. X. Dou, *Angew. Chem., Int. Ed.* **2020**, *132*, 12174.

[48] H. Li, X. Chen, T. Jin, W. Bao, Z. Zhang, L. Jiao, *Energy Storage Mater.* **2019**, *16*, 383.

[49] M. Chen, L. Chen, Z. Hu, Q. Liu, B. Zhang, Y. Hu, Q. Gu, J. L. Wang, L. Z. Wang, X. Guo, S. L. Chou, S. X. Dou, *Adv. Mater.* **2017**, *29*, 1605535.

[50] Y. Xu, Q. Wei, C. Xu, Q. Li, Q. An, P. Zhang, J. Sheng, L. Zhou, L. Mai, *Adv. Energy Mater.* **2016**, *6*, 1600389.

[51] H. Gao, Y. Li, K. Park, J. B. Goodenough, *Chem. Mater.* **2016**, *28*, 6553.

[52] Y. Jiang, J. Liu, *Energy Environ. Mater.* **2019**, *2*, 30.

[53] F. E. M. N. K. Nag, *J. Catal.* **1990**, *124*, 127.

[54] A. E. Esther Bailón-García, F. Ribeiro, C. Henriques, A. F. Pérez-Cadenas, F. Carrasco-Marín, F. J. Maldonado-Hódar, *Carbon* **2020**, *156*, 194.

[55] S. F. Geoffrey, C. Bond, *Appl. Catal.* **1989**, *46*, 89.

[56] J. G. Chen, C. M. Kirn, B. Frühberger, B. D. DeVries, M. S. Touvelle, *Surf. Sci.* **1994**, *321*, 145.

[57] R. M. L. T. P. Moffat, R. R. Ruf, *Electrochim. Acta* **1995**, *40*, 1723.